A Teleconnection between the West Siberian Plain and the ENSO Region

STEFAN LIESS

Department of Earth Sciences, University of Minnesota, Minneapolis, Minnesota

SAURABH AGRAWAL

Department of Computer Science and Engineering, University of Minnesota, Minneapolis, Minnesota

SNIGDHANSU CHATTERJEE

Department of Statistics, University of Minnesota, Minneapolis, Minnesota

VIPIN KUMAR

Department of Computer Science and Engineering, University of Minnesota, Minneapolis, Minnesota

(Manuscript received 14 December 2015, in final form 21 July 2016)

ABSTRACT

The Walker circulation is linked to extratropical waves that are deflected from the Northern Hemisphere polar regions and travel southeastward over central Asia toward the western Pacific warm pool during northern winter. The wave pattern resembles the east Atlantic–west Russia pattern and influences the El Niño–Southern Oscillation (ENSO) region. A tripole pattern between the West Siberian Plain and the two centers of action of ENSO indicates that the background state of ENSO with respect to global sea level pressure (SLP) has a significant negative correlation to the West Siberian Plain. The correlation with the background state, which is defined by the sum of the two centers of action of ENSO, is higher than each of the pairwise correlations with either of the ENSO centers alone. The centers are defined with a clustering algorithm that detects regions with similar characteristics. The normalized monthly SLP time series for the two centers of ENSO (around Darwin, Australia, and Tahiti) are area averaged, and the sum of both regions is considered as the background state of ENSO. This wave train can be detected throughout the troposphere and the lower stratosphere. Its origins can be traced back to Rossby wave activity triggered by convection over the subtropical North Atlantic that emanates wave activity toward the West Siberian Plain. The same wave train also propagates to the central Pacific Ocean around Tahiti and can be used to predict the background state over the ENSO region. This background state also modifies the subtropical bridge between tropical eastern Pacific and subtropical North Atlantic leading to a circumglobal wave train.

1. Introduction

Interannual variations of the climate over the tropical Pacific are dominated by El Niño–Southern Oscillation (ENSO) and the low-frequency variability of ENSO is often attributed to the Pacific decadal oscillation (PDO). El Niño (La Niña) patterns are stronger and more consistent during the positive (negative) phase of the PDO (Gershunov and Barnett 1998). The empirical orthogonal function (EOF) calculation for the PDO index is restricted to the North Pacific (20°–70°N), but the spatial pattern of sea surface temperature (SST) anomalies associated with the PDO is similar to that associated with ENSO (Deser et al. 2010, their Fig. 10) except for the relative weighting between the northern and tropical Pacific. The amplitudes of the SST anomalies in the equatorial eastern Pacific for the PDO are comparable with those in the North Pacific but they are weaker than the ENSO signal (Zhang et al. 1997; Dettinger et al. 2000; Deser et al. 2004, 2010).

The PDO is stronger influencing the eastern part of the Walker circulation over the central and eastern

Pacific (Gershunov and Barnett 1998; Verdon and Franks 2006; Deser et al. 2010) than the western part. A similar relationship exists between the Walker circulation and the North Pacific Gyre Oscillation (Chhak et al. 2009; Di Lorenzo et al. 2010), which is predominantly an ocean response to large-scale atmospheric forcing over the North Pacific. An anomalous lower-tropospheric anticyclone (cyclone) located in the western North Pacific bridges the warm (cold) ENSO events in the eastern Pacific and the weak (strong) East Asian winter monsoon (EAWM) (Wang et al. 2000). However, Wang et al. (2008) point out that the phase of the PDO should be taken into account in the ENSO-based prediction of wintertime climate over East Asia. The ENSO impact on the EAWM is stronger when the PDO is in its negative phase. Also, rainfall and crop yields over Australia are more predictable during the negative PDO period (Power et al. 1999). However, interannual hydroclimate variations in central Asia are more significant during the positive PDO phase (Fang et al. 2014). Thus, the PDO can be described as a background state for decadal ENSO variability such as the recent shift from low-frequency eastern Pacific El Niño events toward higher-frequency central Pacific El Niño events (Kim et al. 2009; Kug et al. 2009; Xie et al. 2015).

ENSO-related eastward propagating Rossby waves produce generally wetter (drier) conditions over North America during El Niño (La Niña) events (Ropelewski and Halpert 1986; Trenberth and Guillemot 1996), but more refined results can be obtained by taking spatial ENSO characteristics into account (Larkin and Harrison 2005) and investigating the combined effect of ENSO and the Pacific–North American (PNA) pattern (Garfinkel and Hartmann 2008). Similarly, although El Niño events are generally accompanied by negative North Atlantic Oscillation (NAO) periods (Gouirand and Moron 2003; Brönnimann et al. 2007), this relationship is mostly true for El Niño events with maximum SST anomalies over the central Pacific, whereas El Niño events with maximum SST anomalies over the eastern Pacific can even contribute to positive NAO periods (Graf and Zanchettin 2012).

Traditionally, the stationary patterns in wave trains that encompass planetary-scale regions have been described as teleconnections (e.g., Wallace and Gutzler 1981; Barnston and Livezey 1987). These teleconnections with frequencies of 10–60 days are often identified as main contributors to blocking patterns. For example, during boreal summer 2010, a strong eastern European blocking and its quasi-stationary wave structure was supported by a combination of a La Niña event and an enhanced polar Arctic dipole mode (Schneidereit et al. 2012). Wave trains that commenced over both the North Pacific and North Atlantic propagated toward eastern

Europe and the polar region, and continued southeastward toward South Asia (Schneidereit et al. 2012). The latter is the east Atlantic–west Russia (EA–WR) pattern (Krichak and Alpert 2005) that was originally referred to as the Eurasia-2 pattern (Barnston and Livezey 1987). Its planetary-scale impacts can even be related to vegetation productivity over the Amazon region (Gonsamo et al. 2015).

Here, we introduce an SLP-based index that describes the background state of the ENSO region and shows how this background state is connected to the West Siberian Plain via a Rossby wave train. Similar to the PDO, this wave train can be used to predict the atmospheric state over the ENSO region and the preferences for the spatial distribution of ENSO activity. However, it should be noted that the slowly evolving oceanic PDO index does not constrain the atmospheric variability in subsequent months (Kumar et al. 2013). The significance of mean SLP anomalies over the West Siberian Plain on Northern Hemispheric climate has previously been described by Smoliak and Wallace (2015), but their analysis has not focused on interactions with tropical climate.

Section 2 of this paper introduces the statistical method used to identify the relationship between the West Siberian Plain and the ENSO region, and the physical mechanisms that govern this relationship are described in section 3. Section 4 links this relationship to a circumglobal wave pattern over the Northern Hemisphere and the results are summarized and discussed in section 5.

2. Identification of tripole patterns

This study uses detrended multiyear monthly mean anomalies of the National Centers for Environmental Prediction (NCEP)–U.S. Department of Energy (DOE) Reanalysis-2 (NCEP-2) SLP data (Kanamitsu et al. 2002) and alternatively the Modern-Era Retrospective Analysis for Research and Applications (MERRA) SLP data (Rienecker et al. 2011) for December–February (DJF) during 1979–2014. MERRA SLP data were interpolated to the $2.5° \times 2.5°$ horizontal resolution of NCEP-2 and both datasets were normalized by dividing SLP over each grid point with its respective temporal standard deviation. This normalization reduces the stronger SLP variability over high and midlatitudes compared to low latitudes. The SLP data have been detrended to reduce the influence of multidecadal oscillations and long-term climate change, which are unlikely initiated by atmospheric Rossby wave activity. Positive long-term SLP trends over the West Siberian Plain and negative trends over eastern Europe and eastern Canada would have contributed to negative correlations (Simmonds 2015, his Fig. 7). Long-term

SLP trends over the equatorial region are much lower (Gillett and Stott 2009, their Fig. 1).

In this study, we define tripole patterns as patterns that comprise of three regions R1, R2, and R3 with their corresponding normalized and area-averaged SLP time series denoted by T1, T2, and T3 respectively, such that T3 shows a stronger correlation with T1 + T2 compared to the correlations between T1 and T3 and between T2 and T3. As a result, a tripole captures a relationship between R3 and the area comprising the combined regions R1 and R2, which is stronger than the two individual relationships between R3 and R1 and between R3 and R2. The strength of a tripole is measured as the correlation between T1 + T2 and T3. For normalized time series where all the three pairwise correlations between R1, R2, and R3 are negative, the combined correlation can be directly computed using the following relation:

$$\mathrm{corr}(T1 + T2, T3) = \frac{\mathrm{corr}(T1, T3) + \mathrm{corr}(T2, T3)}{\sqrt{2[1 + \mathrm{corr}(T1, T2)]}}. \quad (1)$$

As seen in Eq. (1), the negative correlation, or strength, of a tripole increases as the absolute values of each of the three pairwise negative correlations increases. A detailed proof is discussed in the appendix.

To detect negative tripoles, we use a graph-based approach (Kawale et al. 2011, 2013; Liess et al. 2014) that has been used to identify pairs of negatively correlated regions. Such pairs can be found by graph-based methods without requiring a priori region selection or imposing an orthogonality constraint, as in singular value decomposition (SVD) or EOF analysis (Newman and Sardeshmukh 1995; Dommenget and Latif 2002).

Our method to find tripoles consists of two steps. In the first step, pairs of negatively correlated regions are found, and in the second step, we search for all the regions that show a negative correlation with both ends of the initial pair of regions.

Within a global SLP dataset, first all pairs of grid points that are strongly negatively correlated with each other are identified as initial centers of the regions R1 and R2. R1 and R2 are then constructed such that all grid points in R1 and R2 show 1) a positive correlation of 0.85 or larger with their corresponding centers and 2) a negative correlation of −0.3 or lower with at least one of the grid points in the opposite region.

In the second step, for each pair (R1, R2) found above, grid points that are most negatively correlated with a grid point in either of the two regions R1 or R2 are used as centers for regions R3. R3 contains grid points that have 1) a positive correlation of 0.85 or larger with their center and 2) a negative correlation of −0.15

or lower with at least one of the grid points in either region R1 or R2. All the grid points included in R3 are then excluded from being selected as centers of subsequent regions and step 2 is repeated to obtain multiple candidates for R3. Only those triplets of regions R1, R2, and R3 are considered as tripoles where 1) the correlation between R1 + R2 and R3 is statistically significant, 2) a substantial improvement exists in the strength of correlation between R1 + R2 and R3 compared to R1 and R3 and to R2 and R3, respectively, and 3) each of the three regions consists of at least 40 grid points. In the NCEP-2 SLP dataset, this algorithm identifies 124 tripoles including parts of the PNA pattern, but many tripoles can be classified as either spurious or overlapping with previously detected regions. If the correlation thresholds change from 0.85 to 0.8 and from −0.15 to −0.2, the algorithm identifies 178 tripoles in very similar locations. The alternative regions corresponding to the index described in the next section are shown in Fig. S1a in the supplemental material. Additional details about the algorithm can be found in Agrawal et al. (2015). A detailed discussion about the statistical significance of the correlation thresholds based on field significance (Wilks 2006, 2016) and a multiple testing correction for the false discovery rate (FDR; Benjamini and Hochberg 1995; Benjamini and Yekutieli 2001) is included in the supplemental material. The algorithm was initially run on NCEP-2 SLP and the tripole patterns discovered were verified on MERRA SLP and Hadley Centre SLP data (HadSLP2; Allan and Ansell 2006).

3. A link between the West Siberian Plain and the ENSO region

Figure 1 shows three regions forming a tripole pattern between the tropical Pacific and the West Siberian Plain during DJF. The background state of ENSO is described by the normalized and area-averaged SLP values over a region in the western Pacific warm pool (green), hereafter named R1, and a region in the central Pacific just south of where the Niño-3.4 and Niño-4 regions overlap (cyan), hereafter named R2. It should be noted that although we identify a tripole pattern, we combine regions R1 and R2 to show their combined relation to the West Siberian Plain (magenta), hereafter named R3. The combination of R1 and R2 describes a background state over the ENSO region that contains information about its area-averaged SLP strength compared to the global average SLP, which varies only by 0.5 hPa (Trenberth 1981). Thus, our definition of a tripole pattern includes an oscillation between R1 and R2 in the Pacific basin, and an oscillation between the combined region R1 + R2 in the Pacific basin and a third region R3 outside the Pacific
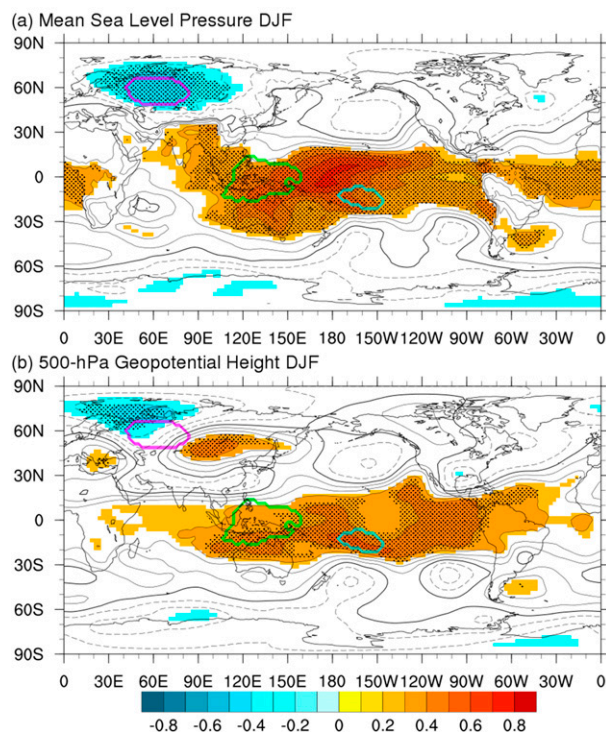
FIG. 1. MERRA SLP tripole between the western Pacific warm pool (R1; green), the central Pacific (R2; cyan), and the West Siberian Plain (R3; magenta) during DJF. Contours indicate the correlation values of (a) SLP and (b) 500-hPa geopotential height with the R1 + R2 time series. Contour interval is 0.1. The zero line is thickened and negative contours are dashed. Statistically significant correlations at the local 95% confidence level are shaded. Stippling shows global field significance based on the FDR approach with $\alpha_{FDR} = 0.1$.

basin. Traditional methods to measure atmospheric ENSO characteristics mostly rely on the SLP difference between Tahiti and Darwin, Australia, and do not take the SLP difference between the ENSO region and the extratropics into account. For DJF, normalized and area-averaged SLP over R3 shows a strong negative correlation with the above defined ENSO background state, which is the sum of normalized and area-averaged SLP values over R1 and R2 (Fig. 1a). Shading in Fig. 1 shows the local 95% confidence level ($\alpha_{global} = 0.05$) based on the Student's t test. Stippling indicates global field significance based on the FDR approach as in Wilks [2016, his Eq. (3) and Fig. 4] with $\alpha_{FDR} = 2\alpha_{global} = 0.1$. This approach is also explained in the supplemental material.

The West Siberian Plain is a low-lying area located between the Ural Mountains to the west, the Central Siberian Plateau to the east, and the Kazakh hill country and the Altai Mountains to the south. Southward propagating anomalies from the West Siberian Plain are considered precursors for sand storms over northwestern China and Mongolia (Jia et al. 2012; Li et al. 2013).

Positive SLP anomalies over the equatorial Pacific and negative anomalies over the West Siberian Plain as shown in Fig. 1a indicate favorable conditions for strong El Niño events between 1958 and 1998 when the 3-month running mean Niño-3.4 SST anomalies exceed one standard deviation and anomalies greater than 0.5°C persist for at least 8 months as described in Wang et al. (2000, their Fig. 4a). These conditions include westerly wind bursts to the north and south of the equator along the isobars of the western Pacific high pressure system (Philander and Pacanowski 1981; Fedorov et al. 2015) but also display a connection to low pressure anomalies over the West Siberian Plain. In this paper, we show results for MERRA reanalysis data. To provide a more comprehensive analysis, results for the NCEP-2 reanalysis are made available in the supplemental material and correlation values for HadSLP2 anomalies for 1850–2012 are included in the text below.

For SLP during DJF, a significant connection at the 95% confidence interval exists between R1 and R3 for MERRA (NCEP-2, HadSLP2) with a correlation of −0.33 (−0.35, −0.31). R1 is significantly correlated to R2 at −0.52 (−0.43, −0.50), which describes the ENSO pattern in the Walker circulation. Although these relationships suggest a positive correlation between R2 and R3, the actual correlation values are slightly negative at −0.12 (−0.21, −0.17). Furthermore, when adding together R1 and R2, the correlation of their sum to R3 strengthens to −0.47 (−0.52, −0.48). These results lead to the definition of the background state of the Walker circulation and the related ENSO signal that is described by the combined SLP pattern over both the western and central Pacific. This extra information allows us to identify a strong significant relationship between the West Siberian Plain and the ENSO region. However, for other seasons and the whole year, we do not find significant correlations of the time series over R3 to R1, R2, or their sum.

The correlation of the R1 + R2 SLP time series to 500-hPa geopotential height (Fig. 1b) reveals a northwestward tilt with height of the negative correlation pattern, which is now centered over the island of Novaya Zemlya in the Arctic Ocean. Additionally, a positive correlation southwest of Lake Baikal emerges. Together with a nonsignificant negative correlation over southern China, these peaks form a wave train from the West Siberian Plain to the western Pacific warm pool around R1.

Figure 2a depicts the time series for R1 + R2 SLP anomalies. Positive peaks of more than 2 times the standard deviation (marked with asterisks) occur mostly before or during eastern Pacific El Niño events, whereas negative peaks are generally associated with central Pacific El Niño events (see Yu and Kim 2013, their Table 1).
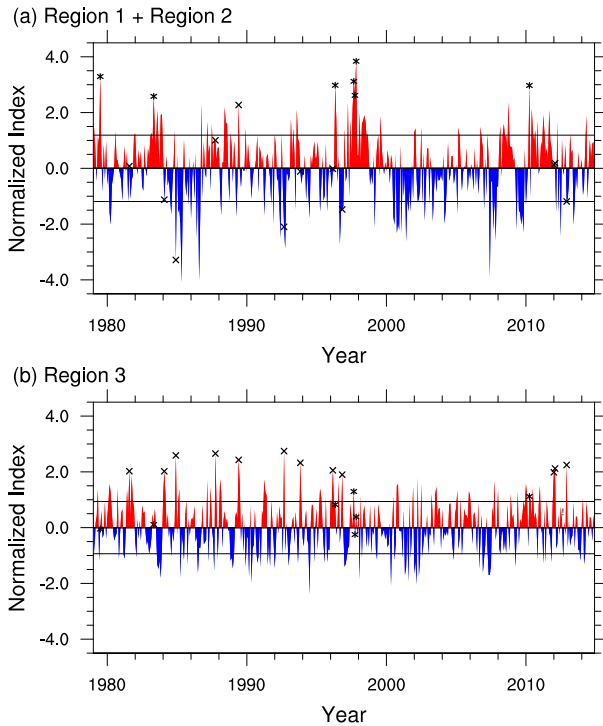
(a) Region 1 + Region 2

(b) Region 3

FIG. 2. Time series of MERRA SLP divided by its standard deviation for (a) area averages over R1 + R2 with asterisks indicating values above two standard deviations and (b) the area average over R3 with crosses indicating values above two standard deviations. Marks for each time series are shown in both time series for easier comparison. Horizontal lines indicate plus and minus one standard deviation.

The positive peaks of more than 2 times the standard deviation in R3 are marked with crosses. During the positive R3 peaks of December 1984, June 1989, September 1992, November 1996, and December 2012, the related R1 + R2 values are outside one standard deviation. Only the June 1989 value relates to a positive R1 + R2 value. The same markers are applied to the R3 time series (Fig. 2b). Since most of the R1 + R2 markers do not correspond to peaks in the R3 time series, it is suggested that the R1 + R2 regions do not play a big role in the signal detected over the R3 region. In contrast, Fig. 2a suggests that positive peaks over the R3 region may be influencing the negative peaks over the R1 + R2 regions during northern fall and winter. Positive peaks of more than 1.5 times the standard deviation corroborate the above result with two-thirds of the peaks in R3 occurring during negative R1 + R2 phases and 10 (4) peaks occurring outside the negative (positive) R1 + R2 standard deviation mostly during boreal winter (summer) months (Fig. S10 in the supplemental material).

Composite maps of geopotential height fields in Figs. 3 and 4 include the temporally averaged pattern of

all positive minus all negative monthly events outside one standard deviation as detected in the R1 + R2 time series in Fig. 2a. Here, we refer to these average patterns outside one standard deviation as positive and negative phases of the wave activity. The dates that contribute to the positive and negative phases are listed in Table S1 in the supplemental material. Composites also display the northward shift of the center of action with height over the R3 region during DJF. Regions with locally significant differences between the positive and negative phase are identified with the Student's t test at a 95% confidence interval (shaded in Figs. 3 and 4) and global field significance that corrects for spatial autocorrelation is based on the FDR approach with $\alpha_{FDR} = 0.1$ (stippling in Figs. 3 and 4). The 850-hPa geopotential height pattern during DJF in Fig. 3a resembles the SLP correlation pattern in Fig. 1a. The strongest negative amplitudes occur over the West Siberian Plain and Novaya Zemlya, and strong positive amplitudes occur over the R1 and R2 regions, similar to the eastern Pacific El Niño phase minus the central Pacific El Niño phase (Graf and Zanchettin 2012, their Fig. 3, right panel).

The composite pattern during JJA (Fig. 3b) reveals statistically significant positive connections throughout central Asia from the West Siberian Plain to the tropical Pacific indicating a nonlinear significant relationship that cannot be found with linear correlation (not shown) but is corroborated by the positive relation during June 1989 (see Fig. 2a). The composite pattern also shows a negative connection over the Ross Sea near Antarctica. At 500 hPa, the four peaks of the wave train are depicted during DJF (Fig. 3c). Compared to DJF, these peaks are shifted westward during JJA starting with a negative center northwest of Norway, positive centers over the West Siberian Plain and the tropical Pacific, and a small nonsignificant negative peak over the Hindu Kush (Fig. 3d). However, there is no apparent vertical tilt in the JJA geopotential height pattern, suggesting the occurrence of a stationary wave during this season. In general, the relationship between R1 + R2 and R3 has a seasonal dependence that can influence the sign of its correlation. The transitional seasons of MAM and SON show similar characteristics to DJF, but the patterns are less significant (not shown).

4. A circumglobal wave train

Geopotential height fields in the upper troposphere and the lower stratosphere (Fig. 4) corroborate the results of Fig. 3. Amplitudes are generally stronger at these levels (please note the different contour intervals in Figs. 3 and 4) and the tropical atmosphere is less significantly impacted. However, although Figs. 4a and 4c indicate the interplay
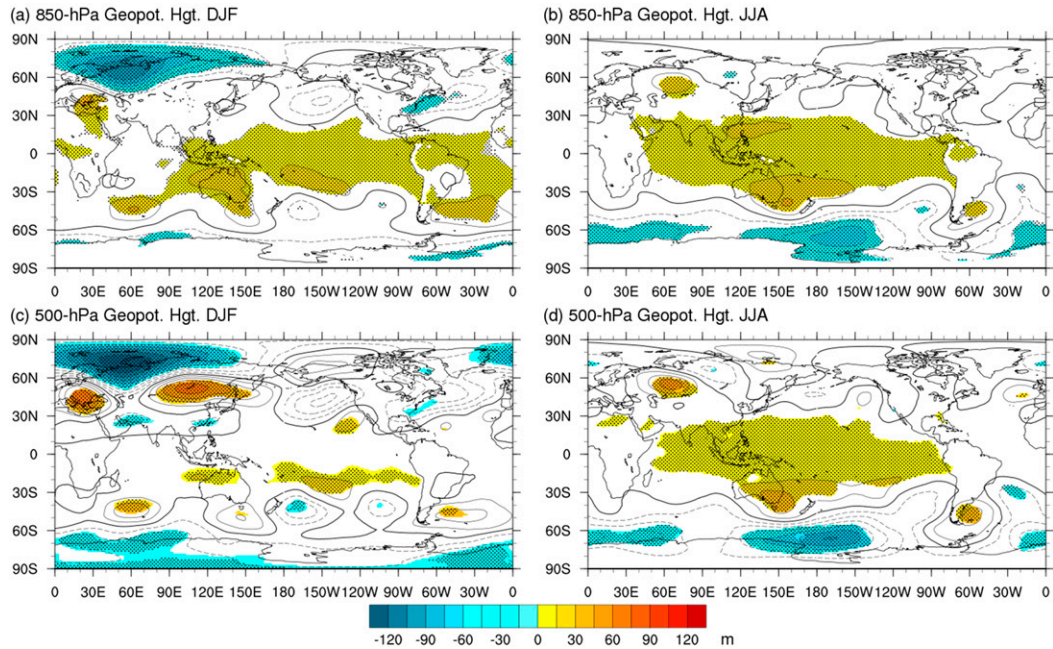
FIG. 3. MERRA geopotential height (m) composite analysis at (a),(b) 850 hPa and (c),(d) 500 hPa for positive minus negative index phases based on seasonal one-standard-deviation thresholds of the time series over R1 + R2 during DJF and JJA, respectively. Contour interval is 15 m. The zero line is thickened and negative contours are dashed. Shading indicates significance using a local Student's *t* test at the 95% confidence level. Stippling shows global field significance based on the FDR approach.

between the wave trains in the upper troposphere and the lower stratosphere with significant differences over the Arctic Ocean near Novaya Zemlya and southwest of Lake Baikal at the 300-hPa level, differences over individual grid points in the 70-hPa level are not significant when corrected with the FDR approach due to the stronger variability in the lower stratosphere. Later in this section, we will show field significance for differences in the zonal
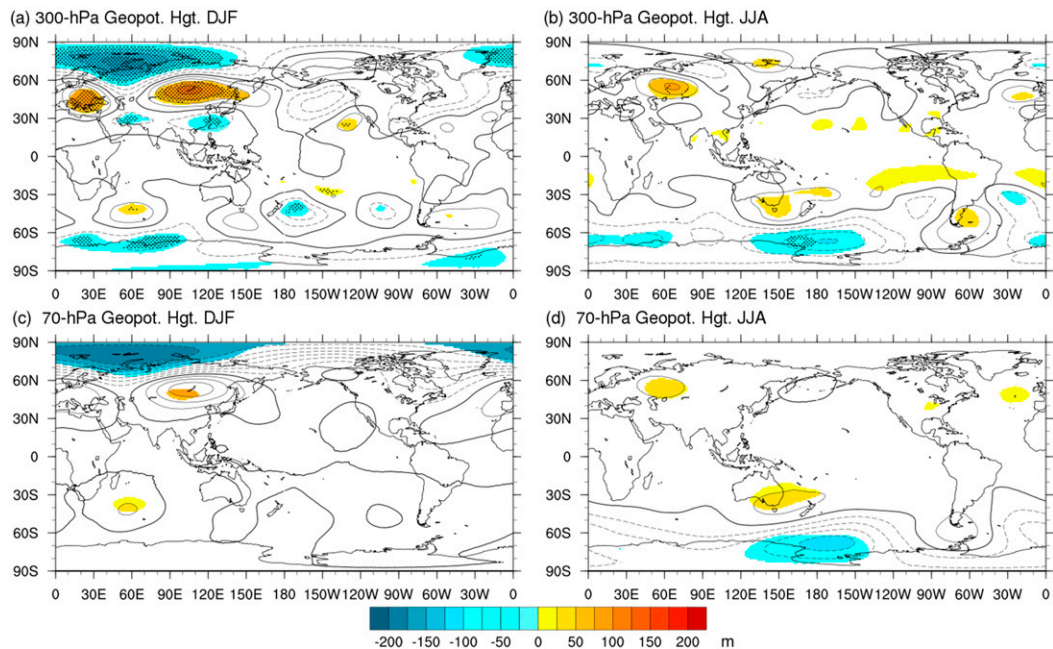

FIG. 4. As in Fig. 3, but for (a),(b) 300-hPa and (c),(d) 70-hPa geopotential height (m). Contour interval is 25 m.

mean zonal wind profile in the lower stratosphere over the centers of action near Novaya Zemlya and Lake Baikal after averaging over 30°-longitude sections. Here, stratosphere–troposphere interaction (Baldwin and Dunkerton 2001; Domeisen et al. 2013; Kunz and Greatbatch 2013) relates to SLP anomalies over the R1 + R2 region. It should be noted that the two positive anomalies over eastern Europe and Lake Baikal indicate the incoming and outgoing ends of a Rossby wave train that is deflected in the northern polar region (Fig. 4a). During JJA, a relationship between the R1 + R2 region and the centers of action of a teleconnection near the Ross Sea and the Tasman Sea shows field significance over a small amount of grid points at 300 hPa. This relationship is also part of the lower- and midtroposphere pattern in Figs. 3b and 3d. The relationship of the teleconnection between the Tasman Sea and the Southern Ocean to the ENSO region has previously been described by Liess et al. (2014). The westward tilt with height of the center over the Ross Sea indicates an eastward propagation along the Antarctic Circumpolar Current around 60°S (e.g., Nowlin and Klinck 1986).

The spatial extrema in 300-hPa streamfunction (Fig. 5) coincide well with extrema in 300-hPa geopotential height in Figs. 4a and 4b. During DJF, the three positive anomalies in the extratropical Northern Hemisphere over eastern Europe around 20°E, over Lake Baikal around 110°E, and over the eastern Pacific around 130°W are connected via the subtropical bridge (Tang and Neelin 2004; Graf and Zanchettin 2012; Park and Dusek 2013) between 90° and 60°W. Please note that the positive anomaly over eastern Europe around 20°E is only significant in geopotential height throughout the troposphere and not in 300-hPa streamfunction after correction with the FDR approach. These anomalies are accompanied by three negative anomalies to the north over Novaya Zemlya, the northeastern Pacific, and the Labrador Sea. Over Eurasia, this pattern indicates a strengthened polar jet stream around 60°N and a weakened East Asian jet stream (EAJS) around 40°N during DJF (see also Ren et al. 2010, their Fig. 1d). The mostly nonsignificant response over the eastern Pacific and North America resembles the positive phase of the PNA pattern (Franzke et al. 2011) and the partly significant pattern between Labrador Sea, Greenland Sea, and the North Atlantic matches the positive phase of the NAO pattern (Feldstein 2003). The linkage of the above patterns results in a circumglobal wave train during northern winter that operates further north than a similar wave train during summer (Ding and Wang 2005).

The direct relationship between EAJS and ENSO is weak in winter (Yang et al. 2002; Gollan et al. 2012) although the EAWM is influenced by both (Wang et al.
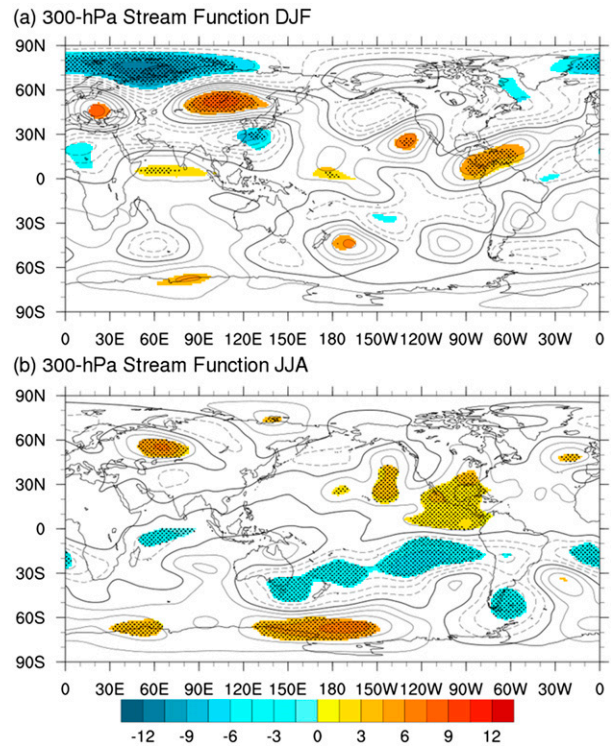

FIG. 5. As in Fig. 3, but for 300-hPa streamfunction ($10^6 \, m^2 \, s^{-1}$) during (a) DJF and (b) JJA. Contour interval is $1.5 \times 10^6 \, m^2 \, s^{-1}$.

2008; Gollan et al. 2012). However, here we show that the wave train from the West Siberian Plain is affecting large parts of the ENSO region that are related to opposite phases of the eastern Pacific and central Pacific El Niño events. A general relation to the ENSO phase is thus difficult to detect. We further suggest that this wave train is the deflection of a poleward propagating Rossby wave train from the subtropical North Atlantic to northwestern Eurasia.

On the decadal scale, Rossby wave activity emanating from the subtropical North Atlantic is influenced by the Atlantic multidecadal oscillation (AMO) (Semazzi et al. 2015). Thus, the present study suggests a link between AMO and the background state of ENSO in the tropical Pacific with the increasingly positive AMO index since the late 1990s being responsible for more wave activity over the northern Atlantic (Dima and Lohmann 2007; Marullo et al. 2011) and thus generally lower eastern Pacific ENSO amplitudes, which is reflected in the increasingly negative phase of the R1 + R2 time series since the late 1990s (Fig. 2a). The AMO signal has a quasi-global impact as shown in model simulations (Zanchettin et al. 2014, their Fig. 3). AMO signals have been detected in observed rainfall over North and South America (Teegavarapu et al. 2013; Kayano and Capistrano 2014) and Australia (Liess et al. 2014). In turn, the ENSO

influence on the AMO has been described by Park and Dusek (2013). They find that the multivariate ENSO index leads the expression of ENSO in the AMO by an average of 6 months.

As already shown in Figs. 3b and 3d, the meridional oscillation between Novaya Zemlya and the Indian Ocean during JJA is weaker and mostly stationary (Fig. 5b). It is suggested that a wave train originates from deep convection in the Indian summer monsoon region, propagates northward, and is then deflected back to the Indian Ocean and the Maritime Continent. This wave train also strengthens the EAJS (see also Ren et al. 2010, their Fig. 1b) as suggested by the negative stream-function anomaly to the north and the positive anomaly to the south between 60° and 120°E (see also Liao et al. 2004, their Fig. 4a). In the Southern Hemisphere, significant negative streamfunction anomalies occur near the R2 region and the eastern Pacific El Niño region over the tropical eastern Pacific cold tongue that may be connected to the subtropical bridge over Central America during JJA.

Figure 6 shows the differences of the positive and negative phases of the three-dimensional wind field during DJF for three longitude sectors over the eastern Atlantic region between 20°W and 10°E, central Asia between 50° and 80°E, and East Asia between 80° and 110°E. Over the eastern Atlantic region (Fig. 6a), the difference in wind pattern between the positive and negative phase is consistent with the difference between the positive and negative northern annular mode (NAM) phase (Limpasuvan and Hartmann 1999; Greatbatch 2000). As mentioned earlier in this section, the averaging over 30°-longitude sections reduces the strong variability in the stratospheric signal identified in Fig. 4c, so that the difference in stratospheric zonal wind north of 60°N is statistically significant after applying the FDR correction with $\alpha_{FDR} = 0.1$. The difference in zonal wind deepens over the Eastern Hemisphere (Figs. 6b,c) where the stratospheric signal propagates downward and generates the equatorward section of the previously described wave train. However, in contrast to the decadal-scale PDO and AMO signals, the wave train described here operates on the monthly to seasonal scale and is connected to the polar stratospheric circulation, similar to the NAM and its variability (Baldwin and Dunkerton 2001; Domeisen et al. 2013; Kunz and Greatbatch 2013). This modification of stratospheric dynamics in turn has been linked to surface temperatures (Cohen et al. 2009) and snowfall (Foster et al. 2013), especially over Siberia (Cohen et al. 2014).

The Eliassen–Palm (EP) flux is used to identify wave propagation between the eastern Atlantic and the West Siberian Plain, and its propagation toward the ENSO region. The EP flux [Edmon et al. 1980, their Eqs. (3.1a)
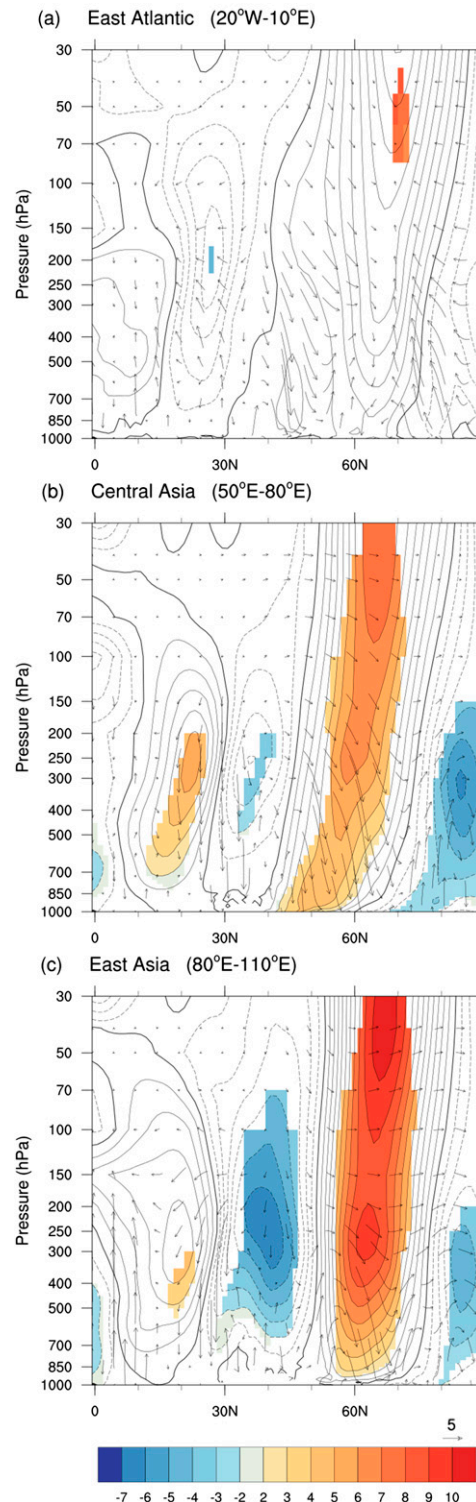

FIG. 6. As in Fig. 3, but for meridional cross sections of zonal wind (contours; m s^{-1}) and meridional circulation (vectors; m s^{-1} and hPa day^{-1}) during DJF over (a) the eastern Atlantic, (b) central Asia, and (c) East Asia. Contour interval is 1 m s^{-1}. Shading indicates global field significance of the differences in zonal wind using the Student's t test and the FDR approach.

and (3.1b)] is calculated from 3-hourly MERRA data. Zonal averages during DJF are compared for the positive and negative phases over the same longitudinal sectors as shown in Fig. 6. The EP flux and its divergence are based on meridional eddy momentum and heat fluxes that indicate wave propagation in the latitude–height cross section. Its divergence describes westerly forcing (Edmon et al. 1980; Andrews 1987). Quasigeostrophic scaling (Andrews et al. 1987) has been used to analyze planetary wave activity. Here, the scaling described in Edmon et al. [1980, their Eq. (3.13)] has been adjusted based on Barsugli (2006):

$$\{\tilde{F}_\phi, \tilde{F}_p\} = \cos\phi \left\{ \frac{F_\phi}{r_0 \pi}, \frac{F_p}{10^5} \right\} \sqrt{\frac{10^5}{p}}, \qquad (2)$$

where ϕ is the latitude, p is the pressure coordinate, r_0 is the radius of Earth, and F_ϕ and F_p are the meridional and vertical components of the EP flux, respectively. Instead of averaging the meridional eddy momentum and heat fluxes over all longitudes, here we compare three subsections of 30° width. Since the wave activity shown in Fig. 7 assumes that the behavior over each 30° subsection occurs on the planetary scale, the depicted values are not scaled to the individual longitude sectors and are thus shown for illustrative purposed only. Furthermore, contours of EP flux divergence are based on spatial interpolation. Green vectors and shaded grid points in Fig. 7 indicate statistical significance at the 95% confidence level for EP flux and EP flux divergence based on a 1000-member Monte Carlo sampling method. Differences in the EP flux are considered significant if either of the two vector components in latitude and height direction is located outside the 95th percentile. Points that are outside the 95th percentile for both phases are only considered as significant if they are located on the opposite ends of the distribution. The 1000 members are generated by randomly selecting a given number of months from both the positive and negative phases. The number of months for each phase is shown in Table S1.

As seen in Figs. 5a and 6a, the positive phase of the R1 + R2 time series represents clockwise anomalies and thus decreased convection in the subtropical Atlantic. In the EP flux around 300 hPa, this is reflected in stronger westerly (easterly) forcing around 45°N (15°N) near western Europe (off the North African coast) between 20°W and 10°E, although only the stronger easterly forcing is indicated by significantly stronger EP flux convergence (Fig. 7a). This lack of convection over the subtropical bridge during the positive phase coincides with increased equatorward heat flux (negative $\tilde{F}_p$) around 30°N in the midtroposphere around 500 hPa.

Also connected to this lack of convection is increased poleward momentum flux (equatorward $\tilde{F}_\phi$) in the lower troposphere around 700 hPa between 30° and 50°N. Similar to the mean wind field in this sector (Fig. 6a), this pattern is consistent with the positive NAM phase (Limpasuvan and Hartmann 1999; Greatbatch 2000). However, the differences in the stratosphere are negligible at these longitudes.

Between 50° and 80°E, the increased poleward momentum flux in the lower troposphere during the positive phase is accompanied by an increased equatorward heat flux in the upper troposphere between 40° and 50°N (Fig. 7c). Poleward momentum as well as heat fluxes are increased in the stratosphere between 40° and 70°N at these longitudes. EP flux divergence in the upper troposphere and the stratosphere indicates that the mean flow receives energy from wave activity, which is consistent with the increased zonal flow around 60°N (Fig. 5a).

Between 80° and 110°E, stratospheric EP flux divergence indicates that westerly forcing is still being generated in the stratosphere during the positive phase (Fig. 7e). However, the poleward heat flux is stronger in the negative phase (Fig. 7f). In the midtroposphere, the increased equatorward heat flux during the positive phase occurs farther south between 15° and 25°N, indicating the southeastward propagation of the detected tropospheric Rossby wave activity.

Figure 8 depicts the global 2-m temperature pattern related to the R1 + R2 index. During DJF, the strongest anomalies of more than ±5 K occur north of Lake Baikal and over the Arctic Ocean northwest of Novaya Zemlya. The strong temperature decrease with increasing latitude during the positive phase strengthens the predominant westerlies in this region. In this phase, the favor for an eastern Pacific El Niño is apparent by the cold anomaly over the western Pacific warm pool and the warm anomaly over the eastern Pacific (only significant in NCEP-2; see Fig. S8a in the supplemental material). The cold anomaly over northern Russia is shifted southeastward to the east of the West Siberian Plain during JJA and the warm anomaly is reduced to a small region to the northeast of the Caspian Sea (Fig. 8b). The cold anomalies over the central Pacific are significant in both reanalysis products during JJA (see Fig. S8b).

Global Precipitation Climatology Project (GPCP; Adler et al. 2003) precipitation anomalies (Fig. 9) show the expected decrease over R1 and R2 during DJF and over R1 during JJA related to positive SLP anomalies. The months found in the NCEP-2 time series (see Fig. S2a in the supplemental material) are also characterized by increased precipitation over the eastern Pacific (see Fig. S9 in the supplemental material), which occurs only in JJA for the MERRA time series (Fig. 9b).
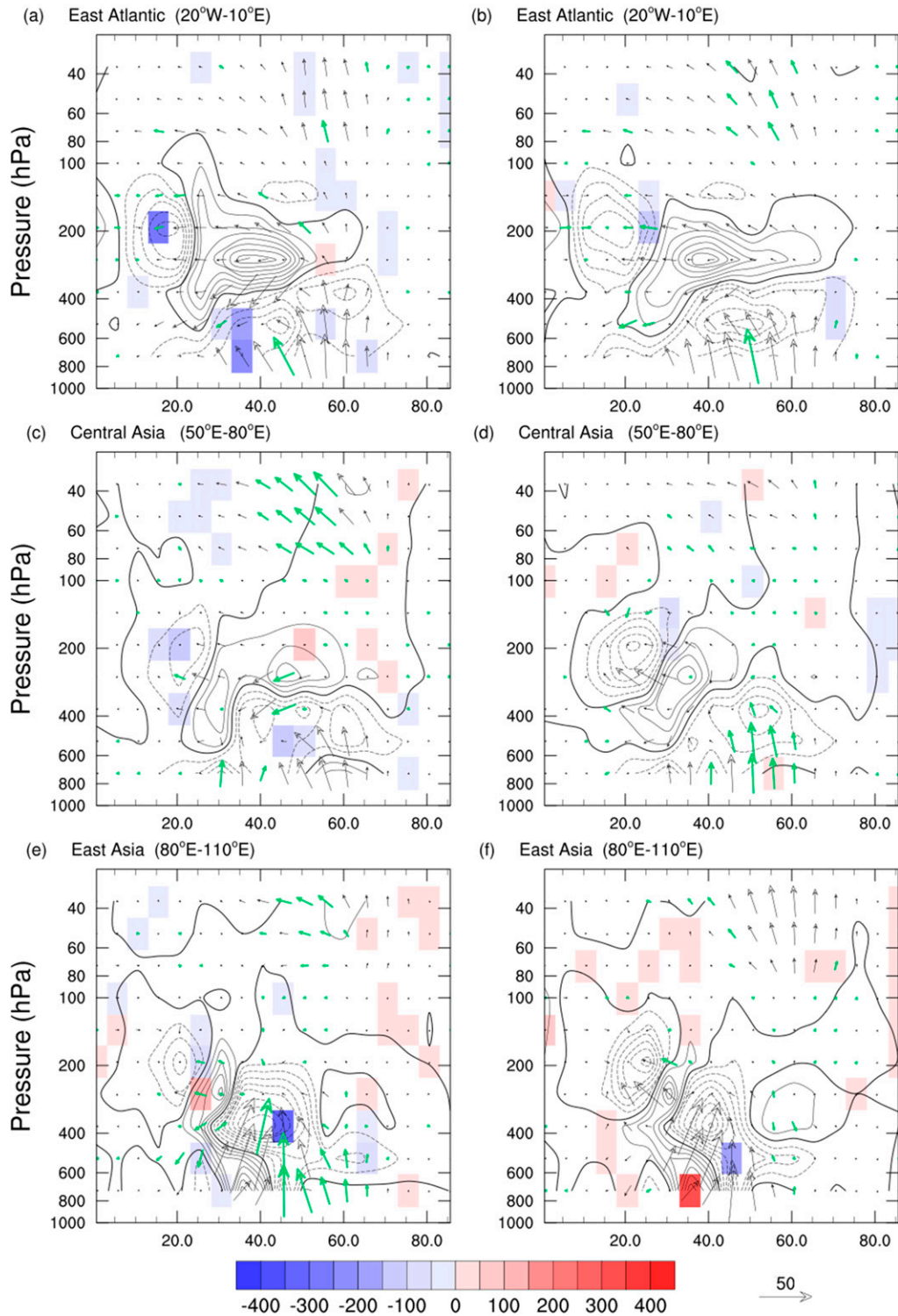
FIG. 7. EP flux ($m^2 s^{-2}$; vectors) and EP flux divergence ($m^2 s^{-2}$; contours) for (left) positive and (right) negative phases of the time series over R1 + R2 averaged over (a),(b) 20°W–10°E, (c),(d) 50°–80°E, and (e),(f) 80°–110°E. Contour interval is 50 $m^2 s^{-2}$, with zero contour thickened and negative contours dashed. Quasigeostrophic scaling has been applied and the EP flux above 100 hPa is magnified by a factor of 5. Thick green vectors and shading indicate statistically significant differences from the median EP flux and EP flux divergence at the 95% confidence level based on 1000-member Monte Carlo sampling.
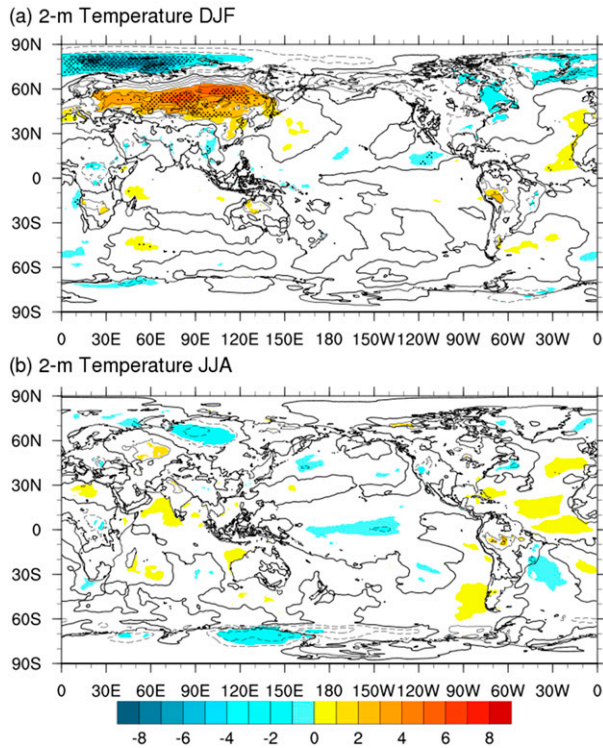
FIG. 8. As in Fig. 3, but for 2-m temperature (°C) during (a) DJF and (b) JJA. Contour interval is 1°C.

FIG. 9. As in Fig. 3, but for GPCP precipitation (mm day^{-1}) during (a) DJF and (b) JJA. Contour interval is 0.5 mm day^{-1}. The zero line is omitted for clarity. Global field significance is indicated by black squares (grid points) in DJF, there is no global field significance during JJA.

However, only the decrease over R2 is statistically significant after the FDR correction. Both reanalysis products show significantly increased winter precipitation over the West Siberian Plain during the positive R1 + R2 phase related to the negative SLP anomalies. Decreased precipitation over the Black Sea and eastern Mediterranean region, which is only statistically significant for months found in the MERRA time series after the FDR correction, results from the significant increase in geopotential height throughout the troposphere (Figs. 3a,c and 4a) that is consistent with the blocking high described in Schneidereit et al. (2012).

5. Summary and conclusions

In this study, we use the MERRA and NCEP-2 reanalysis products to show how the Walker circulation around the western Pacific warm pool and the central Pacific Ocean is influenced by extratropical waves that are deflected from the Northern Hemisphere polar regions during winter and then travel southeastward over central Asia. Although the stationary wave pattern described here roughly resembles the EA–WR pattern, the pattern presented here influences the tropical ENSO region in contrast to the EA–WR pattern, which is confined to the Northern Hemisphere. The positive
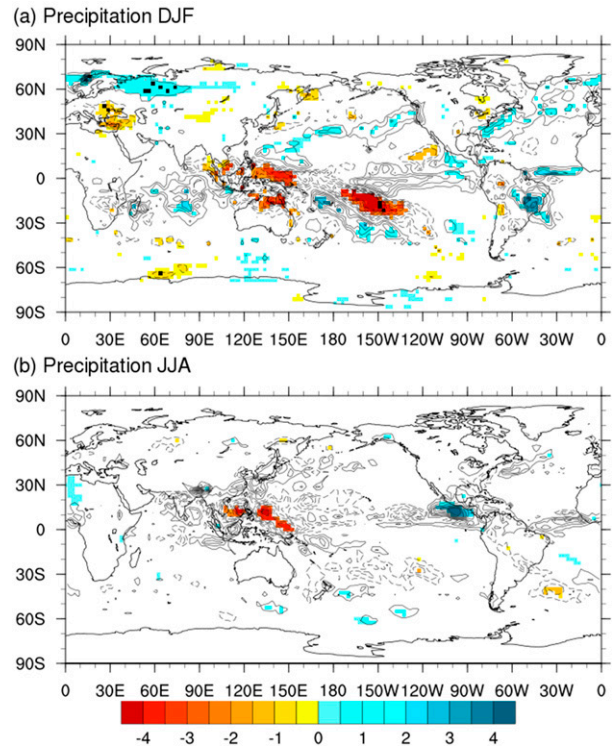
phase of this pattern is defined by two positive peaks over Darwin, Australia, and Tahiti, which are located within the ENSO region. By adding up both ends of the Walker circulation, we remove the signal of its strength, and instead characterize the SLP difference between the ENSO region and the extratropics. This background state of the ENSO region is negatively correlated to an SLP signal over the West Siberian Plain, which exerts Rossby wave activity into the ENSO region. This wave train originates in the subtropical Atlantic and propagates northeastward toward the north of the West Siberian Plain, where it gets deflected southeastward through central Asia and southern East Asia. Two positive anomalies in geopotential height over eastern Europe and Lake Baikal indicate the incoming and outgoing ends of the deflected Rossby wave train and only the outgoing end is significant in the lower stratosphere. This outgoing wave train continues on to the central Pacific Ocean around Tahiti, thus modifying the background state of ENSO.

The analysis of the 300-hPa streamfunction during northern winter indicates that this wave pattern is part of a circumglobal wave train with three significant positive anomalies in the extratropical Northern Hemisphere over eastern Europe, Lake Baikal, and the eastern Pacific.

A fourth positive anomaly over the tropical Pacific and subtropical Atlantic reveals the subtropical bridge (Tang and Neelin 2004; Graf and Zanchettin 2012; Park and Dusek 2013). Negative anomalies exist to the north over Novaya Zemlya, the northeastern Pacific, and the Labrador Sea. Over Eurasia, this pattern indicates a strengthened polar jet stream around 60°N and a weakened East Asian jet stream (EAJS) around 40°N. The positive phase of the above described wave train can also be associated with positive phases of the PNA and NAO patterns. Most prominently however, the association of this circumglobal wave train with the ENSO region indicates that the wave train from the West Siberian Plain is related to opposite phases of the eastern Pacific and central Pacific El Niño events.

A similar but less significant signal can be detected during northern spring and fall (not shown here). During summer, however, the signal of the correlation is reversed and not significant. Only a composite analysis of JJA reanalysis data shows significant patterns of a stationary wave over central and East Asia. The seasonal changes in the detected signal make it difficult to use this signal as a predictive tool and more interpretation is necessary to fully understand the implications of the teleconnections described here.

In general, the AMO influence on Rossby wave activity in the subtropical North Atlantic suggests a multidecadal component in the detected wave train. Hu and Feng (2012) investigated the combined impact of ENSO and AMO on summertime precipitation in North America. The AMO causes an asymmetry in precipitation response to El Niño and La Niña, whereby summertime precipitation has a much larger positive anomaly in El Niño years occurring during the warm phase of the AMO than during the cold phase of the AMO. Although the impact of the detected wave train on regional precipitation is largely confined to the regions R1, R2, and R3, as well as to the Black Sea and eastern Mediterranean region in our analysis, temperature anomalies can be as large as ±5 K north of Lake Baikal and over the Arctic Ocean northwest of Novaya Zemlya. In conclusion, it should be noted that the atmospheric impact on the ENSO region should be taken into account for the characterization of global ENSO signals.

APPENDIX

Combining Correlations

For three normalized time series T_1, T_2, and T_3, each observed over T time stamps, the covariance obeys the identity

$$\mathrm{cov}(T_1 + T_2, T_3) = \mathrm{cov}(T_1, T_3) + \mathrm{cov}(T_2, T_3) \qquad \text{(A1)}$$

(Snedecor and Cochran 1989).

This identity can be used for correlations so that

$$\begin{aligned} &\mathrm{corr}(T_1 + T_2, T_3) \\ &= \frac{\mathrm{cov}(T_1, T_3) + \mathrm{cov}(T_2, T_3)}{\sqrt{\mathrm{var}(T_1) + \mathrm{var}(T_2) + 2\mathrm{cov}(T_1, T_2)}\sqrt{\mathrm{var}(T_3)}}. \end{aligned} \qquad \text{(A2)}$$

Since all time series are normalized, $\mathrm{var}(T_i) = 1$, and thus

$$\begin{aligned} &\mathrm{corr}(T_1 + T_2, T_3) \\ &= \frac{\mathrm{corr}(T_1, T_3) + \mathrm{corr}(T_2, T_3)}{\sqrt{1 + 1 + 2\mathrm{corr}(T_1, T_2)}\sqrt{1}} \quad \text{or} \\ &= \frac{\mathrm{corr}(T_1, T_3) + \mathrm{corr}(T_2, T_3)}{\sqrt{2[1 + \mathrm{corr}(T_1, T_2)]}}. \end{aligned} \qquad \text{(A3)}$$

REFERENCES

Adler, R. F., and Coauthors, 2003: The version-2 Global Precipitation Climatology Project (GPCP) monthly precipitation analysis (1979–present). *J. Hydrometeor.*, **4**, 1147–1167, doi:10.1175/1525-7541(2003)004<1147:TVGPCP>2.0.CO;2.

Agrawal, S., G. Atluri, S. Liess, S. Chatterjee, and V. Kumar, 2015: Tripoles: A new class of climate teleconnections. University of Minnesota Department of Computer Science and Engineering Tech. Rep. TR 15-020, 22 pp. [Available online at https://www.cs.umn.edu/sites/cs.umn.edu/files/tech_reports/15-020.pdf.]

Allan, R., and T. Ansell, 2006: A new globally complete monthly historical gridded mean sea level pressure dataset (HadSLP2): 1850–2004. *J. Climate*, **19**, 5816–5842, doi:10.1175/JCLI3937.1.

Andrews, D. G., 1987: On the interpretation of the Eliassen-Palm flux divergence. *Quart. J. Roy. Meteor. Soc.*, **113**, 323–338, doi:10.1002/qj.49711347518.

——, F. W. Taylor, and M. E. McIntyre, 1987: The influence of atmospheric waves on the general circulation of the middle atmosphere. *Philos. Trans. Roy. Soc. London*, **323A**, 693–705, doi:10.1098/rsta.1987.0115.

Baldwin, M. P., and T. J. Dunkerton, 2001: Stratospheric harbingers of anomalous weather regimes. *Science*, **294**, 581–584, doi:10.1126/science.1063315.

Barnston, A. G., and R. E. Livezey, 1987: Classification, seasonality and persistence of low-frequency atmospheric circulation patterns. *Mon. Wea. Rev.*, **115**, 1083–1126, doi:10.1175/1520-0493(1987)115<1083:CSAPOL>2.0.CO;2.

Barsugli, J., 2006: EP fluxes. NOAA/ESRL Physical Sciences Division. [Available online at http://www.esrl.noaa.gov/psd/data/epflux/.]

Benjamini, Y., and Y. Hochberg, 1995: Controlling the false discovery rate: A practical and powerful approach to multiple testing. *J. Roy. Stat. Soc.*, **57B**, 289–300. [Available online at http://www.jstor.org/stable/2346101.]

——, and D. Yekutieli, 2001: The control of the false discovery rate in multiple testing under dependency. *Ann. Stat.*, **29**, 1165–1188, doi:10.1214/aos/1013699998.

Brönnimann, S., E. Xoplaki, C. Casty, A. Pauling, and J. Luterbacher, 2007: ENSO influence on Europe during the last centuries. *Climate Dyn.*, **28**, 181–197, doi:10.1007/s00382-006-0175-z.

Chhak, K. C., E. Di Lorenzo, N. Schneider, and P. F. Cummins, 2009: Forcing of low-frequency ocean variability in the northeast Pacific. *J. Climate*, **22**, 1255–1276, doi:10.1175/2008JCLI2639.1.

Cohen, J., M. Barlow, and K. Saito, 2009: Decadal fluctuations in planetary wave forcing modulate global warming in late boreal winter. *J. Climate*, **22**, 4418–4426, doi:10.1175/2009JCLI2931.1.

——, J. C. Furtado, J. Jones, M. Barlow, D. Whittleston, and D. Entekhabi, 2014: Linking Siberian snow cover to precursors of stratospheric variability. *J. Climate*, **27**, 5422–5432, doi:10.1175/JCLI-D-13-00779.1.

Deser, C., A. S. Phillips, and J. W. Hurrell, 2004: Pacific interdecadal climate variability: Linkages between the tropics and the North Pacific during boreal winter since 1900. *J. Climate*, **17**, 3109–3124, doi:10.1175/1520-0442(2004)017<3109:PICVLB>2.0.CO;2.

——, M. A. Alexander, S.-P. Xie, and A. S. Phillips, 2010: Sea surface temperature variability: Patterns and mechanisms. *Annu. Rev. Mar. Sci.*, **2**, 115–143, doi:10.1146/annurev-marine-120408-151453.

Dettinger, M. D., D. R. Cayan, G. J. McCabe, and J. A. Marengo, 2000: Multiscale streamflow variability associated with El Niño/Southern Oscillation. *El Niño and the Southern Oscillation: Multiscale Variability and Global and Regional Impacts*, H. F. Diaz and V. Markgraf, Eds., Cambridge University Press, 113–146.

Di Lorenzo, E., K. M. Cobb, J. C. Furtado, N. Schneider, B. T. Anderson, A. Bracco, M. A. Alexander, and D. J. Vimont, 2010: Central Pacific El Niño and decadal climate change in the North Pacific Ocean. *Nat. Geosci.*, **3**, 762–765, doi:10.1038/ngeo984.

Dima, M., and G. Lohmann, 2007: A hemispheric mechanism for the Atlantic multidecadal oscillation. *J. Climate*, **20**, 2706–2719, doi:10.1175/JCLI4174.1.

Ding, Q., and B. Wang, 2005: Circumglobal teleconnection in the Northern Hemisphere summer. *J. Climate*, **18**, 3483–3505, doi:10.1175/JCLI3473.1.

Domeisen, D. I. V., L. Sun, and G. Chen, 2013: The role of synoptic eddies in the tropospheric response to stratospheric variability. *Geophys. Res. Lett.*, **40**, 4933–4937, doi:10.1002/grl.50943.

Dommenget, D., and M. Latif, 2002: A cautionary note on the interpretation of EOFs. *J. Climate*, **15**, 216–225, doi:10.1175/1520-0442(2002)015<0216:ACNOTI>2.0.CO;2.

Edmon, H. J., B. J. Hoskins, and M. E. McIntyre, 1980: Eliassen–Palm cross sections for the troposphere. *J. Atmos. Sci.*, **37**, 2600–2616, doi:10.1175/1520-0469(1980)037<2600:EPCSFT>2.0.CO;2.

Fang, K., F. Chen, A. K. Sen, N. Davi, W. Huang, J. Li, and H. Seppä, 2014: Hydroclimate variations in central and monsoonal Asia over the past 700 years. *PLoS One*, **9**, e102751, doi:10.1371/journal.pone.0102751.

Fedorov, A. V., S. Hu, M. Lengaigne, and E. Guilyardi, 2015: The impact of westerly wind bursts and ocean initial state on the development, and diversity of El Niño events. *Climate Dyn.*, **44**, 1381–1401, doi:10.1007/s00382-014-2126-4.

Feldstein, S. B., 2003: The dynamics of NAO teleconnection pattern growth and decay. *Quart. J. Roy. Meteor. Soc.*, **129**, 901–924, doi:10.1256/qj.02.76.

Foster, J. L., J. Cohen, D. A. Robinson, and T. W. Estilow, 2013: A look at the date of snowmelt and correlations with the Arctic Oscillation. *Ann. Glaciol.*, **54**, 196–204, doi:10.3189/2013AoG62A090.

Franzke, C., S. B. Feldstein, and S. Lee, 2011: Synoptic analysis of the Pacific–North American teleconnection pattern. *Quart. J. Roy. Meteor. Soc.*, **137**, 329–346, doi:10.1002/qj.768.

Garfinkel, C. I., and D. L. Hartmann, 2008: Different ENSO teleconnections and their effects on the stratospheric polar vortex. *J. Geophys. Res.*, **113**, D18114, doi:10.1029/2008JD009920.

Gershunov, A., and T. P. Barnett, 1998: Interdecadal modulation of ENSO teleconnections. *Bull. Amer. Meteor. Soc.*, **79**, 2715–2725, doi:10.1175/1520-0477(1998)079<2715:IMOET>2.0.CO;2.

Gillett, N. P., and P. A. Stott, 2009: Attribution of anthropogenic influence on seasonal sea level pressure. *Geophys. Res. Lett.*, **36**, L23709, doi:10.1029/2009GL041269.

Gollan, G., R. J. Greatbatch, and T. Jung, 2012: Tropical impact on the East Asian winter monsoon. *Geophys. Res. Lett.*, **39**, L17801, doi:10.1029/2012GL052978.

Gonsamo, A., J. M. Chen, and P. D'Odorico, 2015: Underestimated role of east Atlantic–west Russia pattern on Amazon vegetation productivity. *Proc. Natl. Acad. Sci. USA*, **112**, E1054–E1055, doi:10.1073/pnas.1420834112.

Gouirand, I., and V. Moron, 2003: Variability of the impact of El Niño–Southern Oscillation on sea-level pressure anomalies over the North Atlantic in January to March (1874–1996). *Int. J. Climatol.*, **23**, 1549–1566, doi:10.1002/joc.963.

Graf, H.-F., and D. Zanchettin, 2012: Central Pacific El Niño, the "subtropical bridge," and Eurasian climate. *J. Geophys. Res.*, **117**, D01102, doi:10.1029/2011JD016493.

Greatbatch, R. J., 2000: The North Atlantic Oscillation. *Stochastic Environ. Res. Risk Assess.*, **14**, 213–242, doi:10.1007/s004770000047.

Hu, Q., and S. Feng, 2012: AMO- and ENSO-driven summertime circulation and precipitation variations in North America. *J. Climate*, **25**, 6477–6495, doi:10.1175/JCLI-D-11-00520.1.

Jia, L.-H., H.-Y. Li, R.-Q. Li, H. Tang, and W. Huo, 2012: Numerical simulation and diagnosis analysis of "3.12" sandstorm in south Xinjiang. *J. Desert Res.*, **32**, 1135–1141. [Available online at http://zgsm.westgis.ac.cn/EN/abstract/abstract2258.shtml.]

Kanamitsu, M., W. Ebisuzaki, J. Woollen, S.-K. Yang, J. J. Hnilo, M. Fiorino, and G. L. Potter, 2002: NCEP–DOE AMIP-II reanalysis (R-2). *Bull. Amer. Meteor. Soc.*, **83**, 1631–1643, doi:10.1175/BAMS-83-11-1631.

Kawale, J., M. Steinbach, and V. Kumar, 2011: Discovering dynamic dipoles in climate data. *Proc. 2011 SIAM Int. Conf. on Data Mining*, Philadelphia, PA, Society for Industrial and Applied Mathematics, 107–118, doi:10.1137/1.9781611972818.10.

——, and Coauthors, 2013: A graph-based approach to find teleconnections in climate data. *Stat. Anal. Data Min.*, **6**, 158–179, doi:10.1002/sam.11181.

Kayano, M. T., and V. B. Capistrano, 2014: How the Atlantic multidecadal oscillation (AMO) modifies the ENSO influence on the South American rainfall. *Int. J. Climatol.*, **34**, 162–178, doi:10.1002/joc.3674.

Kim, H.-M., P. J. Webster, and J. A. Curry, 2009: Impact of shifting patterns of Pacific Ocean warming on North Atlantic tropical cyclones. *Science*, **325**, 77–80, doi:10.1126/science.1174062.

Krichak, S. O., and P. Alpert, 2005: Decadal trends in the east Atlantic–west Russia pattern and Mediterranean precipitation. *Int. J. Climatol.*, **25**, 183–192, doi:10.1002/joc.1124.

Kug, J.-S., F.-F. Jin, and S.-I. An, 2009: Two types of El Niño events: Cold tongue El Niño and warm pool El Niño. *J. Climate*, **22**, 1499–1515, doi:10.1175/2008JCLI2624.1.

Kumar, A., H. Wang, W. Wang, Y. Xue, and Z.-Z. Hu, 2013: Does knowing the oceanic PDO phase help predict the atmospheric anomalies in subsequent months? *J. Climate*, **26**, 1268–1285, doi:10.1175/JCLI-D-12-00057.1.

Kunz, T., and R. J. Greatbatch, 2013: On the northern annular mode surface signal associated with stratospheric variability. *J. Atmos. Sci.*, **70**, 2103–2118, doi:10.1175/JAS-D-12-0158.1.

Larkin, N. K., and D. E. Harrison, 2005: On the definition of El Niño and associated seasonal average U.S. weather anomalies. *Geophys. Res. Lett.*, **32**, L13705, doi:10.1029/2005GL022738.

Li, Y.-P., G. Dele, Q. Si, and X.-H. Wu, 2013: A synoptic analysis on forecasting of sand-dust storm in November over Inner Mongolia. *J. Desert Res.*, **33**, 1483–1491. [Available online at http://zgsm.westgis.ac.cn/EN/abstract/abstract2550.shtml.]

Liao, Q.-H., S.-Y. Tao, and H.-J. Wang, 2004: Interannual variation of summer subtropical westerly jet in East Asia and its impacts on the climate anomalies of East Asia summer monsoon. *Chin. J. Geophys.*, **47**, 12–21, doi:10.1002/cjg2.449.

Liess, S., and Coauthors, 2014: Different modes of variability over the Tasman Sea: Implications for regional climate. *J. Climate*, **27**, 8466–8486, doi:10.1175/JCLI-D-13-00713.1.

Limpasuvan, V., and D. L. Hartmann, 1999: Eddies and the annular modes of climate variability. *Geophys. Res. Lett.*, **26**, 3133–3136, doi:10.1029/1999GL010478.

Marullo, S., V. Artale, and R. Santoleri, 2011: The SST multidecadal variability in the Atlantic–Mediterranean region and its relation to AMO. *J. Climate*, **24**, 4385–4401, doi:10.1175/2011JCLI3884.1.

Newman, M., and P. D. Sardeshmukh, 1995: A caveat concerning singular value decomposition. *J. Climate*, **8**, 352–360, doi:10.1175/1520-0442(1995)008<0352:ACCSVD>2.0.CO;2.

Nowlin, W. D., Jr., and J. M. Klinck, 1986: The physics of the Antarctic Circumpolar Current. *Rev. Geophys.*, **24**, 469–491, doi:10.1029/RG024i003p00469.

Park, J., and G. Dusek, 2013: ENSO components of the Atlantic multidecadal oscillation and their relation to North Atlantic interannual coastal sea level anomalies. *Ocean Sci.*, **9**, 535–543, doi:10.5194/os-9-535-2013.

Philander, S. G. H., and R. C. Pacanowski, 1981: Response of equatorial oceans to periodic forcing. *J. Geophys. Res.*, **86**, 1903–1916, doi:10.1029/JC086iC03p01903.

Power, S., T. Casey, C. Folland, A. Colman, and V. Mehta, 1999: Inter-decadal modulation of the impact of ENSO on Australia. *Climate Dyn.*, **15**, 319–324, doi:10.1007/s003820050284.

Ren, X., X. Yang, and C. Chu, 2010: Seasonal variations of the synoptic-scale transient eddy activity and polar front jet over East Asia. *J. Climate*, **23**, 3222–3233, doi:10.1175/2009JCLI3225.1.

Rienecker, M. M., and Coauthors, 2011: MERRA: NASA's Modern-Era Retrospective Analysis for Research and Applications. *J. Climate*, **24**, 3624–3648, doi:10.1175/JCLI-D-11-00015.1.

Ropelewski, C. F., and M. S. Halpert, 1986: North American precipitation and temperature patterns associated with the El Niño/Southern Oscillation (ENSO). *Mon. Wea. Rev.*, **114**, 2352–2362, doi:10.1175/1520-0493(1986)114<2352:NAPATP>2.0.CO;2.

Schneidereit, A., S. Schubert, P. Vargin, F. Lunkeit, X. Zhu, D. H. W. Peters, and K. Fraedrich, 2012: Large-scale flow and the long-lasting blocking high over Russia: Summer 2010. *Mon. Wea. Rev.*, **140**, 2967–2981, doi:10.1175/MWR-D-11-00249.1.

Semazzi, F., and Coauthors, 2015: Decadal variability of the East African monsoon. *CLIVAR Exchanges*, No. 66, International CLIVAR Project Office, Southampton, United Kingdom, 15–19. [Available online at http://www.clivar.org/sites/default/files/documents/CLIVAR_Exchanges_No_66_Final_with_bleed_23_June_15.pdf.]

Simmonds, I., 2015: Comparing and contrasting the behaviour of Arctic and Antarctic sea ice over the 35 year period 1979–2013. *Ann. Glaciol.*, **56**, 18–28, doi:10.3189/2015AoG69A909.

Smoliak, B. V., and J. M. Wallace, 2015: On the leading patterns of Northern Hemisphere sea level pressure variability. *J. Atmos. Sci.*, **72**, 3469–3486, doi:10.1175/JAS-D-14-0371.1.

Snedecor, G. W., and W. G. Cochran, 1989: *Statistical Methods*. 8th ed. Iowa State University Press, 503 pp.

Tang, B. H., and J. D. Neelin, 2004: ENSO influence on Atlantic hurricanes via tropospheric warming. *Geophys. Res. Lett.*, **31**, L24204, doi:10.1029/2004GL021072.

Teegavarapu, R. S. V., A. Goly, and J. Obeysekera, 2013: Influences of Atlantic multidecadal oscillation phases on spatial and temporal variability of regional precipitation extremes. *J. Hydrol.*, **495**, 74–93, doi:10.1016/j.jhydrol.2013.05.003.

Trenberth, K. E., 1981: Seasonal variations in global sea level pressure and the total mass of the atmosphere. *J. Geophys. Res.*, **86**, 5238–5246, doi:10.1029/JC086iC06p05238.

——, and C. J. Guillemot, 1996: Physical processes involved in the 1988 drought and 1993 floods in North America. *J. Climate*, **9**, 1288–1298, doi:10.1175/1520-0442(1996)009<1288:PPIITD>2.0.CO;2.

Verdon, D. C., and S. W. Franks, 2006: Long-term behaviour of ENSO: Interactions with the PDO over the past 400 years inferred from paleoclimate records. *Geophys. Res. Lett.*, **33**, L06712, doi:10.1029/2005GL025052.

Wallace, J. M., and D. S. Gutzler, 1981: Teleconnections in the geopotential height field during the Northern Hemisphere winter. *Mon. Wea. Rev.*, **109**, 784–812, doi:10.1175/1520-0493(1981)109<0784:TITGHF>2.0.CO;2.

Wang, B., R. Wu, and X. Fu, 2000: Pacific–East Asian teleconnection: How does ENSO affect East Asian climate? *J. Climate*, **13**, 1517–1536, doi:10.1175/1520-0442(2000)013<1517:PEATHD>2.0.CO;2.

Wang, L., W. Chen, and R. Huang, 2008: Interdecadal modulation of PDO on the impact of ENSO on the East Asian winter monsoon. *Geophys. Res. Lett.*, **35**, L20702, doi:10.1029/2008GL035287.

Wilks, D. S., 2006: On "field significance" and the false discovery rate. *J. Appl. Meteor. Climatol.*, **45**, 1181–1189, doi:10.1175/JAM2404.1.

——, 2016: "The stippling shows statistically significant grid-points": How research results are routinely overstated and

overinterpreted, and what to do about it. *Bull. Amer. Meteor. Soc.*, doi:10.1175/BAMS-D-15-00267.1, in press.

Xie, R., F. Huang, F.-F. Jin, and J. Huang, 2015: The impact of basic state on quasi-biennial periodicity of central Pacific ENSO over the past decade. *Theor. Appl. Climatol.*, **120**, 55–67, doi:10.1007/s00704-014-1150-y.

Yang, S., K.-M. Lau, and K.-M. Kim, 2002: Variations of the East Asian jet stream and Asian–Pacific–American winter climate anomalies. *J. Climate*, **15**, 306–325, doi:10.1175/1520-0442(2002)015<0306:VOTEAJ>2.0.CO;2.

Yu, J.-Y., and S. T. Kim, 2013: Identifying the types of major El Niño events since 1870. *Int. J. Climatol.*, **33**, 2105–2112, doi:10.1002/joc.3575.

Zanchettin, D., O. Bothe, W. Müller, J. Bader, and J. H. Jungclaus, 2014: Different flavors of the Atlantic multidecadal variability. *Climate Dyn.*, **42**, 381–399, doi:10.1007/s00382-013-1669-0.

Zhang, Y., J. M. Wallace, and D. S. Battisti, 1997: ENSO-like interdecadal variability: 1900–93. *J. Climate*, **10**, 1004–1020, doi:10.1175/1520-0442(1997)010<1004:ELIV>2.0.CO;2.